

Materialist: Physically Based Editing Using Single-Image Inverse Rendering

Lezhong Wang¹ Duc Minh Tran¹ Ruiqi Cui¹ Thomson TG¹
 Manmohan Chandraker² Jeppe Revall Frisvad¹

¹Technical University of Denmark ²University of California, San Diego
 {lewa, dmitr, ruicu, thtg, jerf}@dtu.dk, mkchandraker@ucsd.edu

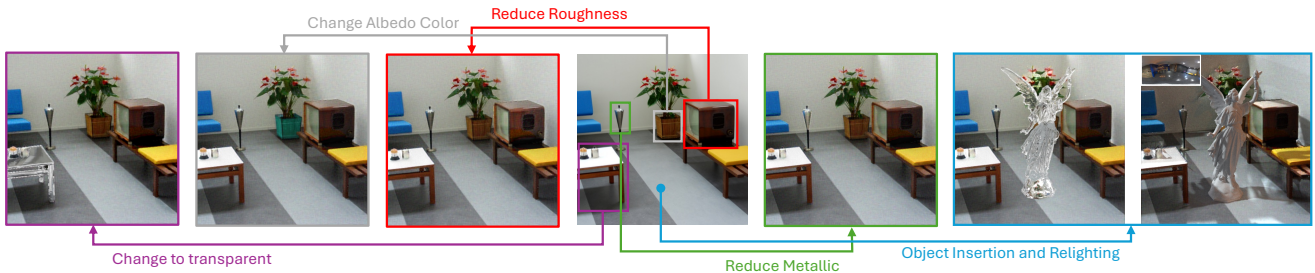


Figure 1. Given an image (in the middle), our inverse rendering approach enables physically based image editing, including transparency, albedo, roughness, metallic, transparent object insertion and relighting. The image is sourced from the IIW dataset [4].

Abstract

To perform image editing based on single-view, inverse physically based rendering, we present a method combining a learning-based approach with progressive differentiable rendering. Given an image, our method leverages neural networks to predict initial material properties. Progressive differentiable rendering is then used to optimize the environment map and refine the material properties with the goal of closely matching the rendered result to the input image. We require only a single image while other inverse rendering methods based on the rendering equation require multiple views. In comparison to single-view methods that rely on neural renderers, our approach achieves more realistic light material interactions, accurate shadows, and global illumination. Furthermore, with optimized material properties and illumination, our method enables a variety of tasks, including physically based material editing, object insertion, and relighting. We also propose a method for material transparency editing that operates effectively without requiring full scene geometry. Compared with methods based on Stable Diffusion, our approach offers stronger interpretability and more realistic light refraction based on empirical results. Code is available at github.com/lez-s/Materialist

1. Introduction

High-quality image editing often requires professional skills. Reducing the complexity and increasing the accuracy of im-

age editing has long been a focus in computer vision and computer graphics [3, 36, 40, 45]. With the success of Stable Diffusion (SD) [48] in image generation, researchers have explored using SD for image editing [7, 19, 38, 77]. However, SD often struggles with precise material property editing. Alchemist [53] attempts to address this by training SD on a large synthetic dataset, but their method lacks interpretability, a physical foundation, and struggles with accurate light refraction for transparent objects.

Inverse rendering offers a promising solution to these challenges. Single-view inverse rendering [28, 29, 52, 79] decomposes images into albedo, roughness, and metallic properties via neural networks (MaterialNet), enhancing interpretability. However, relying on a neural renderer as a substitute for a physically based renderer still shares limitations with SD, such as difficulties in accurately handling of shadows and refraction. Multi-view inverse rendering [1, 2, 30, 67, 69, 71] leverages multi-view constraints and the rendering equation to adhere better to physical principles and achieve superior results. The multi-view input requirement, however, restricts its applicability. Applying differentiable rendering to a single image leads to an ill-posed problem with infinitely many possible solutions.

To address these issues, we adopt a more interpretable inverse rendering approach that combines the strengths of single- and multi-view methods (MaterialNet and the rendering equation). Additionally, we introduce material transparency editing, a capability not previously explored in single-image inverse rendering.

Our main contributions are threefold:

- **Hybrid Approach:** We integrate learning-based methods with differentiable rendering for a hybrid approach applicable to various inverse rendering tasks. To address the infinite optimization possibilities in single-view differentiable rendering, we use neural network-predicted material properties as pseudo ground truth to guide the optimization process.
- **Physically Based Material Editing:** Instead of a neural renderer, our method leverages Mitsuba [20] to achieve physically based material editing with precise global illumination, shadows, and realistic object-environment interactions, thus outperforming existing methods in material editing, relighting, and transparent object insertion tasks.
- **Single-View Transparency Editing:** We propose a single-view, physically based transparency editing method with index of refraction (IOR) and specular transmission, which operates under the single-view constraint without requiring complete geometry or full scene reconstruction.

In addition, we demonstrate that our material prediction model outperforms the latest model based on Stable Diffusion [24] with much faster inference. We also achieve better results in single-view differentiable Monte Carlo ray tracing for environment maps and introduce a mesh reconstruction method well-suited for single-image inverse rendering.

2. Related work

Multi-view inverse rendering. Early work like IPT [1] was limited to simple scenes. They used multi-view constraints and assumed known scene geometry when using the rendering equation for inverse rendering. With NeRF [37], physically based inverse rendering with multi-view images became more feasible [2, 30, 56, 69, 71]. In addition, use of differentiable Monte Carlo rendering led to better shape and material estimation [18, 33, 64, 67, 73, 76], but these techniques still rely on multi-view inputs. More recent methods employ neural networks as renderers for multi-view inputs [12], bypassing computational optimization but currently lacking the performance of equation-based methods in material editing and object insertion. Like most multi-view techniques, our approach uses the rendering equation but requires only a single-view image as input.

Single-view inverse rendering. Unlike multi-view inverse rendering, which relies on the rendering equation, single-view inverse rendering often uses neural networks trained on large datasets to replace physically based rendering [26, 27, 29, 34, 49, 52, 79]. A neural network usually called MaterialNet, predicts material properties (albedo, roughness, metallic) and per-pixel lighting from a single image, which are then used for image synthesis. Although neural renderers perform well in specific tasks like human face relighting [41, 70], they struggle with generalist tasks

where physical simulation is more accurate such as material editing and transparent object insertion. Unless trained on a well represented dataset, the neural renderers fall apart.

In differentiable rendering, early studies addressed rasterization non-differentiability [10, 11], while recent work has explored inverse Monte Carlo ray tracing [14, 21, 75], similar to our physics-based optimization. However, these methods require significant priors and are limited to single objects, making them less suitable for complex scenes. Our approach also uses MatNet for single-view material property inference but incorporates a physics-based renderer.

Material Editing. Material editing generally follows two categories. The first involves inferring material properties through inverse rendering, then modifying them to achieve edits [1, 25, 78]. These methods provide strong interpretability, and using a physics-based renderer makes results highly reliable, though realism may sometimes be limited. The second set is neural network-based. Following the success of Stable Diffusion [48], many image editing methods have emerged [7, 38, 55, 63]. Alchemist [53] is a representative example, trained on synthetic data to allow editing of albedo, roughness, metallic properties, and transparency. These methods benefit from the strengths of Stable Diffusion and achieve highly realistic results but have limited interpretability due to their neural network-based nature. Our approach falls into the first category with a solid interpretability, meanwhile, it enables realistic results.

Light Estimation. Light estimation is a distinct research field [13, 16, 42, 57, 58, 60, 62, 72]. Some methods represent lighting implicitly [24, 69, 78], limiting generalizability, while others require multi-view inputs and scene mesh data [42, 60, 72]. DPI [35] is related to our approach. This method combines differential rendering with Stable Diffusion for high-quality envmap generation but relies on multi-view NeRF methods for mesh reconstruction and lacks material BRDF data, reducing accuracy. In contrast, our approach uses MatNet’s output for more accurate envmap optimization.

Shadows and Ray Tracing. Shadows are crucial for photorealistic rendering. Previous work by Li et al. [29] emphasized shadow accuracy, using an OptiX-based ray tracer [43] to compute shadows for neural network input. However, shadows are often neglected in recent research [30, 69, 78]; methods based on screen-space or image-based ray tracing lack geometric occlusion and thus fail to generate accurate shadows [24, 69, 78]. Many neural renderers struggle with shadow generation [12, 79], as accurate shadows require physically based light transport, it is worth noting that this limitation has been utilized to identify AI-generated

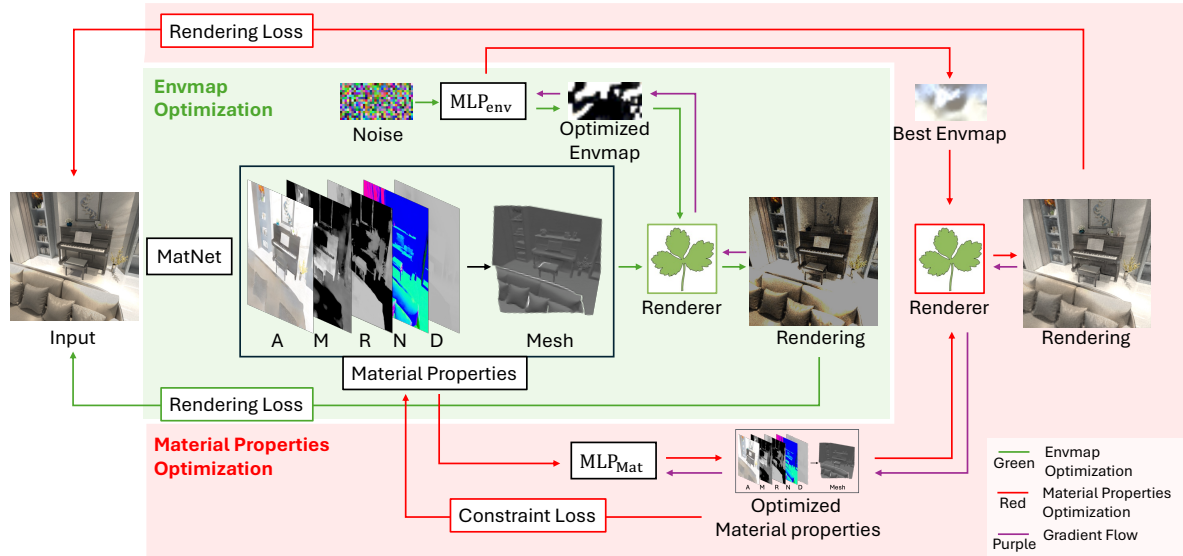


Figure 2. Our inverse rendering pipeline. Given an image, we use MatNet to predict material properties, followed by envmap optimization to estimate the lighting. We then perform material properties optimization, using the envmap that yields the smallest \mathcal{L}_{re} during envmap optimization as the light source. The losses \mathcal{L}_{re} and \mathcal{L}_{cons} guide this process, allowing \mathcal{L}_{re} to be minimized while keeping the results close to the MatNet predictions. See Sec. 3.2 for further details.

images [50]. Our method includes full path tracing for physically accurate shadows.

3. Method

Our material estimation and editing framework consists of four main steps. For relighting, only the geometry reconstruction and the material prediction network (Sec. 3.1) are needed. Object insertion and material editing on the other hand require all four steps, including mesh reconstruction. We assume a pinhole camera model with a 35-degree field of view, $w \times h = 512 \times 512$ image resolution, and $c = 3$ color channels.

3.1. Material Prediction Network

Due to the significant success of Stable Diffusion [48] in image generation, recent work used it for the task of material property estimation, achieving impressive results [24]. However, this approach comes with high training costs and requires computationally intensive multi-step sampling during prediction. In comparison, we found that the model architecture for depth estimation [68] aligns more closely with the requirements of material prediction. We therefore adopt the DPT architecture [46], which has been highly successful in depth estimation, for our material prediction task. Different from [79], we utilize a pretrained DINOv2 [39] encoder for feature extraction. Like previous research in depth estimation [6, 68], we use two DPT decoders [46] for the regression of depth and material properties, respectively. Given the advancements in depth estimation, we initialize our training with weights from the pretrained depth

model [68] to expedite the training process. For the DPT depth decoder, we limit training to the last four layers of the refinenet, while the weights of the DINOv2 encoder remain frozen throughout the training. The following loss function for \mathcal{L}_{MatNet} is used to optimize the model,

$$\mathcal{L}_{MatNet} = \sum_{i \in \{A, R, M, N, D\}} \mathcal{L}_i, \quad (1)$$

where the albedo loss \mathcal{L}_A combines the LPIPS perceptual loss and L_1 loss, while both the roughness loss \mathcal{L}_R and metallic loss \mathcal{L}_M are measured using the L_1 loss between the predictions and ground truth values. Finally, the \mathcal{L}_D is calculated using SiLogLoss [5, 15] to introduce logarithmic error and keep its scale constant to improve the robustness of depth prediction. This loss is defined by

$$\mathcal{L}_D = \sqrt{\mathbb{E}_{i \in \text{mask}} \left((\log(t_i) - \log(p_i))^2 \right) - \lambda \left(\mathbb{E}_{i \in \text{mask}} (\log(t_i) - \log(p_i)) \right)^2}, \quad (2)$$

where t_i is the ground truth and p_i is the predicted depth value for the valid pixel i , and we use $\lambda = 0.5$ as the hyperparameter that balances the variance and mean terms. To prevent outliers in the depth map from causing the model to collapse during training, we set the mask to a depth value in $[0, 20]$. Finally, \mathcal{L}_N is calculated using cosine similarity.

The prediction process of the neural network can be expressed as

$$\mathbf{A}_p, \mathbf{R}_p, \mathbf{M}_p, \mathbf{N}_p, \mathbf{D}_p = \text{MatNet}(I), \quad (3)$$

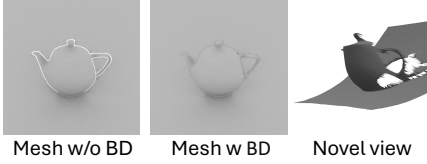


Figure 3. Our single-view mesh reconstruction method used on a test scene. Our method eliminates the white border at the edges. However, since our approach is based on the depth map, it primarily reconstructs the front view of the scene.

where $\mathbf{A}_p, \mathbf{R}_p, \mathbf{M}_p, \mathbf{N}_p, \mathbf{D}_p$ represent the albedo, roughness, metallic, normal, and depth predicted by MatNet and I is the input image.

Mesh Reconstruction. Using \mathbf{D}_p , 2D pixels are projected into 3D to form a point cloud, and neighboring pixels are connected to create a triangle mesh. This method produces a single connected component, which is unsuitable for multi-object scenes. To address this, we identify boundary points by checking the inequality: $\arcsin(\vec{n} \cdot \vec{v}) < \tau$, where \vec{n} is the triangle’s normal, \vec{v} is the view direction, and τ (default 3 degrees) is an angular threshold. Vertices satisfying this condition are marked as boundary points, which are further projected with the depth of the nearest non-boundary pixel. A final pass removes triangles connecting different objects, which unfortunately leads to white borders around foreground objects. To resolve this, we introduce boundary duplication (BD) mesh reconstruction, where new vertices share the 2D coordinates of the foreground boundary but use background depth, effectively eliminating borders. See Fig. 3 as an example.

3.2. Progressive Differentiable Rendering

Our method assumes ambient lighting, represented by an environment map, and does not explicitly model light sources within the scene. Ignoring emitters in the scene, the rendering equation becomes the reflected radiance equation:

$$L_o(\mathbf{x}, \vec{\omega}_o) = \int_{\Omega} f_r(\mathbf{x}, \vec{\omega}_i, \vec{\omega}_o) L_i(\mathbf{x}, \vec{\omega}_i) (\vec{\omega}_i \cdot \vec{n}) d\omega_i, \quad (4)$$

where $L_o(\mathbf{x}, \vec{\omega}_o)$ is the outgoing radiance at the world space position \mathbf{x} in the direction $\vec{\omega}_o$, $f_r(\mathbf{x}, \vec{\omega}_i, \vec{\omega}_o)$ is the bidirectional reflectance distribution function (BRDF) at \mathbf{x} , representing the ratio of reflected radiance in the direction $\vec{\omega}_o$ to irradiance from the direction $\vec{\omega}_i$, while $L_i(\mathbf{x}, \vec{\omega}_i)$ is the incident radiance at \mathbf{x} from the direction $\vec{\omega}_i$, \vec{n} is the surface normal at \mathbf{x} , and Ω is the hemisphere around \vec{n} covering all directions of incidence. We let $\mathbf{S}(\mathbf{x}) = \mathbf{x}_s$ denote the transformation from world space to screen space coordinates. Detailed steps are in the supplementary material.

Simplified DisneyBRDF. To model surface scattering we use the DisneyBRDF [8, 9] for our implementation. During

the optimization process, we do not model sheen, clearcoat, and glass, so the BRDF in Eq. 4 can be written

$$f_r(\mathbf{x}, \vec{\omega}_i, \vec{\omega}_o) = f_s + (1 - \mathbf{M}(\mathbf{x}_s)) f_d \quad (5)$$

with the specular (f_s) and diffuse (f_d) terms defined by

$$f_s = \frac{F_s(\vec{\omega}_i, \vec{\omega}_o; \eta) D_s(\vec{h}; \mathbf{R}(\mathbf{x}_s)) G_s(\vec{\omega}_i, \vec{\omega}_o; \mathbf{R}(\mathbf{x}_s))}{4 |\vec{n} \cdot \vec{\omega}_i| |\vec{n} \cdot \vec{\omega}_o|} \quad (6)$$

$$f_d = \frac{\mathbf{A}(\mathbf{x}_s)}{\pi} F_d(\vec{\omega}_i) F_d(\vec{\omega}_o), \quad (7)$$

where F is the Fresnel reflectance, which here uses the half vector $\vec{h} = (\vec{\omega}_i + \vec{\omega}_o) / \|\vec{\omega}_i + \vec{\omega}_o\|$ and models the fraction of light reflected from the surface as a function of material properties, including the relative index of refraction η . We use the modified Schlick approximation [8]:

$$F_s(\vec{\omega}_i, \vec{\omega}_o; \eta) = C_0(\eta) + (1 - C_0(\eta))(1 - \vec{h} \cdot \vec{\omega}_o)^5 \quad (8)$$

$$C_0(\eta) = R_0(\eta)(1 - \mathbf{M}(\mathbf{x}_s)) + \mathbf{M}(\mathbf{x}_s) \mathbf{A}(\mathbf{x}_s), \quad (9)$$

where $R_0(\eta)$ is the Fresnel reflectance of a dielectric at normal incidence. Similarly, for the diffuse term,

$$F_d(\vec{\omega}) = 1 + (F_{D90} - 1)(1 - \vec{n} \cdot \vec{\omega})^5 \quad (10)$$

$$F_{D90} = 0.5 + 2 \mathbf{R}(\mathbf{x}_s) (\vec{h} \cdot \vec{\omega})^2. \quad (11)$$

Regarding the other terms, D_s is the microfacet normal distribution function, while G_s is the microfacet shadowing-masking function [51]. We use the GGX distribution [61] for these terms due to its simplicity, with just one roughness parameter $\mathbf{R}(\mathbf{x}_s)$, while being able to fit empirical data well.

Environment Map Optimization. We optimize the environment map \mathbf{E} (envmap) using a position-embedded multi-layer perceptron (MLP), similar to the approach used in NeRF [37]. Although optimizing \mathbf{E} directly without using a neural network is theoretically possible, this often yields sub-optimal results. Standard MLPs are generally insensitive to high-frequency information, making pixel-level optimization of the image difficult; CNNs encounter similar limitations. The envmap is obtained using

$$\mathbf{E} = \text{MLP}_{\text{env}}(\gamma(\mathbf{e}); \theta_{\text{env}}), \quad (12)$$

where $\gamma(\cdot)$ is a positional encoding function and θ_{env} is the set of parameters for the MLP. We use `Softplus` after the final layer in MLP_{env} to ensure that the output has only positive values. The envmap \mathbf{E} and the input image \mathbf{e} are both in $\mathbb{R}^{(w \times h) \times c}$ with the input image being initially noise.

In a differentiable rendering of the geometry $\mathbf{D}_p, \mathbf{N}_p$ based on Monte Carlo integration of Eq. 4, we evaluate the BRDF using $\mathbf{A}_p, \mathbf{R}_p, \mathbf{M}_p$ (Eq. 5) and the incident radiance using

$$L_i(\mathbf{x}, \vec{\omega}_i) = V(\mathbf{x}, \vec{\omega}_i) L_{\mathbf{E}}(\vec{\omega}_i), \quad (13)$$

where $L_{\mathbf{E}}(\vec{\omega}_i)$ is the radiance from the envmap in the direction $\vec{\omega}_i$ and $V(\mathbf{x}, \vec{\omega}_i)$ is visibility, which is zero if geometry is found in the direction $\vec{\omega}_i$ and one otherwise.

Our optimization goal is to find the \mathbf{E}^* that minimizes the difference between the rendering and the ground truth (I):

$$\mathbf{E}^* = \underset{\mathbf{E}}{\operatorname{argmin}} \mathcal{L}_{\mathbf{E}}(L_o(\mathbf{x}, \vec{\omega}_o), I) \quad (14)$$

where environment map loss $\mathcal{L}_{\mathbf{E}}$ combines L_1 and L_2 loss. The network weights θ_{env} are discarded after optimization as we only need \mathbf{E}^* .

Material Properties Optimization. Once we have an optimized envmap we further refine the obtained material properties given in section 4.1 using a position-embedded MLP such that :

$$[\mathbf{A}, \mathbf{R}, \mathbf{M}] = \text{MLP}_{\text{mat}}(\gamma(\mathbf{m}); \theta_{\text{mat}}) \quad (15)$$

$$\mathbf{m} = [\mathbf{A}_p, \mathbf{R}_p, \mathbf{M}_p], \quad (16)$$

where $[\cdot, \cdot]$ denotes a concatenation operation and $\mathbf{m} \in \mathbb{R}^{(w \times h) \times 5}$ after concatenating along the color channel.

We use the following formula as the activation function after the final layer:

$$[\mathbf{A}, \mathbf{R}, \mathbf{M}] = \zeta \tanh(\mathbf{z}) + \mathbf{m}, \quad (17)$$

where \mathbf{z} is the output from the final layer, and ζ is a scaling factor. Unlike regular images, $\mathbf{A}, \mathbf{R}, \mathbf{M}$ may contain many values equal to 0 or 1. Approximating these extremes requires \tanh to output very large or small \mathbf{z} values, which can hinder optimization. The scale factor ζ mitigates this by adjusting the range of \mathbf{z} , facilitating smoother training.

The rendering process is the same as for the envmap, except that now we use \mathbf{E}^* and keep it fixed.

Our optimization goal is to find $\mathbf{A}^*, \mathbf{R}^*, \mathbf{M}^*$ that minimize the difference between the rendered result and the ground truth (I):

$$\mathbf{A}^*, \mathbf{R}^*, \mathbf{M}^* = \underset{\mathbf{A}, \mathbf{R}, \mathbf{M}}{\operatorname{argmin}} \mathcal{L}_{\text{Mat}}(L_o(\mathbf{x}, \vec{\omega}_o), I) \quad (18)$$

where \mathcal{L}_{Mat} is the material loss:

$$\mathcal{L}_{\text{Mat}} = \mathcal{L}_{\text{re}} + \delta \mathcal{L}_{\text{cons}}, \quad (19)$$

and the individual terms are:

$$\mathcal{L}_{\text{re}} = \mathcal{L}_{L_1}(L_o, I) + \mathcal{L}_{L_2}(L_o, I) \quad (20)$$

$$\mathcal{L}_{\text{cons}} = \sum_{X \in \{\mathbf{A}, \mathbf{R}, \mathbf{M}\}} \mathcal{L}_{L_1}(X_o, X_p), \quad (21)$$

where \mathcal{L}_{L_1} and \mathcal{L}_{L_2} represent the L_1 and L_2 losses, respectively, and \mathcal{L}_{re} measures the rendering loss between L_o and

I . The constraint loss $\mathcal{L}_{\text{cons}}$ compares the optimized and predicted material properties, introducing constraints to align the optimization with MatNet’s predictions while minimizing the difference between L_o and I . The scaling factor δ controls the deviation from MatNet predictions: a smaller δ allows more flexibility, while a larger δ keeps the optimization closer to MatNet, potentially increasing the gap between the rendering and the target.

Optimization can be in stages: first optimizing \mathbf{R} and \mathbf{M} , then \mathbf{A} . As albedo impacts rendering most significantly, increasing its scale factor in $\mathcal{L}_{\text{cons}}$ during joint optimization prevents the network from overfocusing on albedo, ensuring balanced material property optimization. Besides, our method can optimize normals, but we found optimizing only \mathbf{A}, \mathbf{R} , and \mathbf{M} yields sufficiently good results, while adding normals degrades performance. See supplementary material for details.

3.3. Opaque Material Editing

For $\mathbf{R}, \mathbf{M}, \mathbf{A}$ edits (excluding transparency), we use the SAM2 [47] model to segment the input image, creating a mask for the edit region. We can then modify values within this region and re-render an image. For \mathbf{A} edits, we convert to HSV color space for intuitive color adjustments.

Material Transparency Editing. As described in Sec. 3.1, we reconstruct the mesh using the depth map, capturing only the visible front side of objects (see Fig. 3). This limits transparent object editing, as refractive effects cannot be fully modeled. While existing methods generate multi-view images for mesh reconstruction via NeRF [31, 32, 37, 54] or Gaussian Splatting [17, 23, 74], we aim to solve Material Transparency Editing directly within a single-view constraints, avoiding full scene reconstruction. We model transparent objects using DisneyBSDF [9] as:

$$f_{\text{glass}} = \frac{\sqrt{\mathbf{A}_{\text{glass}}(\mathbf{x}_s)(1 - F_s)D_s G_s} |\vec{h} \cdot \vec{\omega}_o| |\vec{h} \cdot \vec{\omega}_i|}{|\vec{n} \cdot \vec{\omega}_i| |\vec{n} \cdot \vec{\omega}_o| (\vec{h} \cdot \vec{\omega}_i + \eta \vec{h} \cdot \vec{\omega}_o)^2}, \quad (22)$$

where $\mathbf{A}_{\text{glass}}(\mathbf{x}_s) = (1 - \mathbf{M}(\mathbf{x}_s))\mathbf{A}_{\text{BG}}(\mathbf{x}_s)T$, with T denoting specular transmission and \mathbf{A}_{BG} the albedo of the diffuse background object after refraction (distinct from \mathbf{A}). Thus, by knowing the refraction points, we can simulate transparency effects without a back-side mesh, supporting single-view transparency editing.

We use SAM2 [47] for object mask extraction and an inpainting model [48] to generate \mathbf{A}_{BG} . For an incoming ray of direction $-\vec{\omega}_o$ hitting the masked area, the direction of the transmitted ray $\vec{\omega}_t$ is computed using the law of refraction [22].

Assuming the object’s back normal is same as its front normal $\mathbf{N}_p(\mathbf{x}_s)$, the world position after two refractions is

$$\mathbf{x}_2 = \mathbf{x} + d_1 \vec{\omega}_{t1} + d_2 \vec{\omega}_{t2}, \quad (23)$$

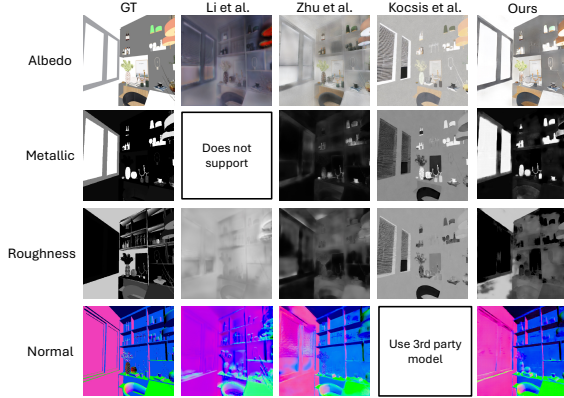


Figure 4. Qualitative results of material prediction on synthetic dataset.

where \mathbf{x} is the initial position of incidence, d_1 and d_2 are refraction distances, and $\vec{\omega}_{t1}$ and $\vec{\omega}_{t2}$ are the directions after first and second refractions, respectively. Note that $\vec{\omega}_{t2}$ depends on $\mathbf{N}_p(\mathbf{S}(\mathbf{x} + d_1 \vec{\omega}_{t1}))$. We trained a neural network on synthetic data to predict d_1 and d_2 for various shapes. Thus, $\mathbf{A}_{BG}(\mathbf{x}_s) = \mathbf{A}_{BG}(\mathbf{S}(\mathbf{x}_2))$, where $\mathbf{S}(\mathbf{x}_2)$ are the screen coordinates of \mathbf{x}_2 after double refraction.

Refraction Length Prediction. We briefly explain the synthetic dataset preparation and training strategy, for more details we refer to the supplementary material.

Dataset Preparation: Due to multiple refractions within the object and varying refraction distances depending on the IOR, we simplify the refraction distance for single transmission when the IOR is approximately 1. For each object, we randomly selected 200 camera positions, pairing each with 200 different envmaps as backgrounds.

Training: We normalize the refraction length to [0,1] and use the object along with its corresponding mask as input, with the refraction length as ground truth, following the same training method used for the depth map.

4. Experiments

This section evaluates the performance of our method.

4.1. Material Prediction Accuracy

Synthetic Dataset. We evaluate the performance of our MatNet on the testset of the InteriorVerse [78] synthetic indoor dataset. As shown in Table 1, our method achieves better prediction accuracy across all evaluated metrics. Qualitative comparisons are shown in Fig. 4.

Real World Dataset. We assess the performance of albedo predictions using the IIW dataset [4], which includes sparse pairwise human annotations for albedo. For evaluation, we use the metric developed for the IIW dataset, Weighted Human Disagreement Rate (WHDR), which quantifies the error



Figure 5. Qualitative results of material prediction on the real world dataset IIW [4]. Zhu et al. [78] retained too many details from the original image while Kocsis et al. [24], due to their reliance on Stable Diffusion, altered image details excessively. Additionally, Kocsis et al.’s method struggles to handle specular highlights and facial features effectively.

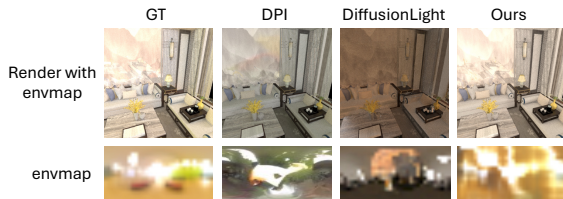


Figure 6. Qualitative results of envmap optimization.

when predicted albedo values differ from human-provided annotations. As shown in Table 2, our model achieves better results with a lower WHDR score. Fig. 5 provides a qualitative comparison.

4.2. Environment Map Optimization

Currently, single-view envmap generation primarily relies on Stable Diffusion [44], which can only produce visually plausible envmaps. Optimization-based methods often require multi-view input [42, 60, 72] or use implicit lighting representations [24, 69, 78]. For optimization approaches, we selected DPI [35] as our benchmark, adapting it to single-view input and providing it with a mesh reconstructed using our method (Sec. 3.1).

As our focus is not high-resolution envmaps, we limit the resolution to 32×16 , consistent with prior work [12, 28]. We evaluated three scenes, each with 60 envmap optimization results. Evaluation metrics included the difference between the optimized and the ground truth envmaps and the difference between relit scenes using the optimized and the ground truth envmaps. Both methods used ground truth material properties for relighting. As shown in Table 1, our method outperformed the others across all metrics, benefiting from the MatNet-predicted properties \mathbf{A}_p , \mathbf{R}_p , \mathbf{M}_p during envmap optimization. Qualitative results are in Fig. 6.

Notably, while rerendering error is low, envmap error remains relatively high due to the inherent ambiguity in single-view optimization; accurate lighting in certain regions

Table 1. Quantitative Evaluation of Material Prediction on Synthetic Dataset [78].

| | Albedo | | | Roughness | | | Metallic | | | Depth | | Normal |
|--------------------|-----------------|-----------------|--------------------|-----------------|-----------------|--------------------|-----------------|-----------------|--------------------|------------------|-------------------|----------------------------------|
| | PSNR \uparrow | SSIM \uparrow | LPIPS \downarrow | PSNR \uparrow | SSIM \uparrow | LPIPS \downarrow | PSNR \uparrow | SSIM \uparrow | LPIPS \downarrow | MAE \downarrow | RMSE \downarrow | Angular Error \downarrow |
| Li et al. [29] | 6.173 | 0.488 | 0.529 | 8.665 | 0.529 | 0.559 | - | - | - | - | - | 37.696 $^\circ$ |
| Zhu et al.[78] | 13.407 | 0.680 | 0.302 | 13.670 | 0.596 | 0.360 | 15.600 | 0.489 | 0.281 | 1.828 | 2.045 | 26.872 $^\circ$ |
| Kocsis et al. [24] | 12.774 | 0.656 | 0.307 | 9.070 | 0.516 | 0.384 | 7.228 | 0.205 | 0.375 | - | - | - |
| Ours | 19.530 | 0.811 | 0.108 | 16.632 | 0.663 | 0.294 | 18.660 | 0.701 | 0.243 | 0.244 | 0.491 | 11.359$^\circ$ |

Table 2. Quantitative evaluation, WHDR ($\delta = 0.1$), of albedo predictions on the IIWild Dataset [4].

| | WHDR \downarrow |
|--------------------|-------------------|
| Li et al. [29] | 0.342 |
| Zhu et al. [78] | 0.232 |
| Kocsis et al. [24] | 0.206 |
| Ours | 0.197 |

Table 3. Quantitative evaluation of environment map optimization. *Envmap* measures the difference between the optimized and ground truth envmaps, while *Rerender* represents the difference between the rendered relit scene with the optimized envmap and the ground truth. SH ERROR calculates the error as the norm of the difference matrix between the spherical harmonics of the ground truth and optimized envmaps. The label *mat* indicates the material properties predicted by MatNet.

| | SSIM \uparrow | | PSNR \uparrow | | MSE \downarrow | | SH ERROR \downarrow |
|---------------------|-----------------|--------------|-----------------|---------------|------------------|--------------|-----------------------|
| | Envmap | Rerender | Envmap | Rerender | Envmap | Rerender | Envmap |
| DiffusionLight [44] | 0.279 | 0.342 | 0.635 | 13.595 | 8.728 | 0.134 | 7.800 |
| DPI [35] | 0.403 | 0.640 | 1.115 | 15.155 | 7.767 | 0.166 | 6.768 |
| Ours w/o mat | 0.414 | 0.518 | 0.902 | 10.242 | 8.302 | 0.355 | 5.571 |
| Ours w/ mat | 0.703 | 0.784 | 4.507 | 18.981 | 6.734 | 0.023 | 3.049 |

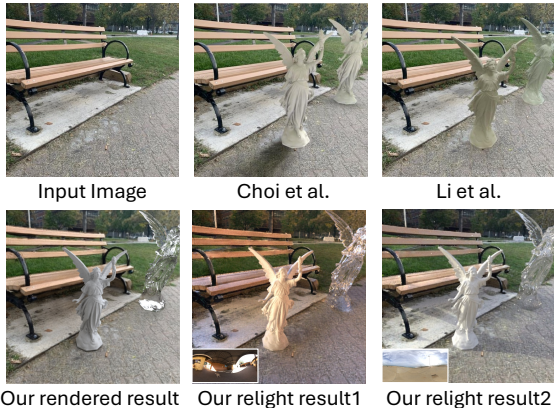


Figure 7. Qualitative results of object insertion and relighting, compared with the multi-view method MAIR (Choi et al. [12]) and the single-view method by Li et al. [27]. Note that relight result2 has a realistic shadow.

can yield a close match to the ground truth, even if the overall envmap differs significantly.

4.3. Object insertion and relighting

Since our rendering process is physically based, it enables the rendering of realistic shadows in object insertion tasks, which significantly enhances the realism of image editing, as seen in Fig. 7.

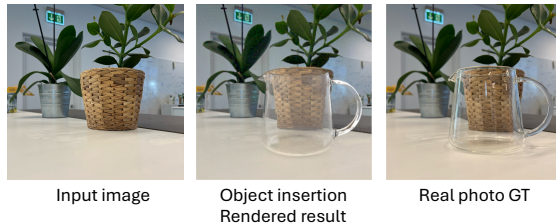


Figure 8. Comparison between ground truth (GT) and our object insertion result for real world image. The error in the reflective area mainly comes from the insufficient accuracy of optimized envmap, as explained in Sec. 4.2.

Additionally, to validate the visual accuracy of our approach, we used real photograph comparisons instead of synthetic data. We 3D scanned a glass jug to obtain its mesh and took photographs of the scene from the same angle with and without the jug. We then inserted the mesh jug into the image without the jug and compared it with the actual photograph, as demonstrated in Fig. 8.

Since single-view inverse rendering mostly uses neural networks for rendering and does not support object insertion of transparent objects, we only compare the difference between ground truth and our method.

4.4. Material Editing

For transparency editing evaluation, we used real-world photo comparisons. A 3D-printed opaque jug, identical in size to the scanned mesh from Sec. 4.3, was placed alongside a glass jug at a fixed camera position, and two photos were captured as ground truth for transparency editing. Since Alchemist [53], closely related to our work, is not open-sourced, we compared our method with iPix2Pix [7] and Stable Diffusion inpainting [48]. For iPix2Pix, text prompts were used for editing, while Stable Diffusion inpainting received both a mask of the jug region and a text prompt. Results are shown in Fig. 9.

For albedo, roughness, and metallic evaluation, since Alchemist [53] is not open-sourced, we extracted images from its paper and applied our material editing for comparison. These images are notably out-of-domain for indoor scenes. While MatNet predicts accurately for indoor scenes, only albedo predictions remain reliable, with roughness and metallic predictions being less consistent. However, differential rendering allows us to perform inverse rendering on real photos using only albedo. To compensate for unreliable roughness and metallic predictions, we manually set priors

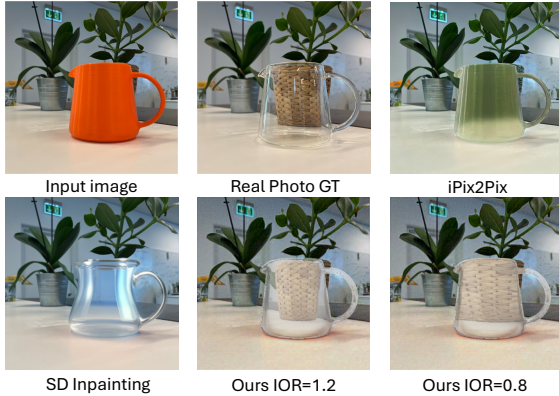


Figure 9. Material transparency editing compared with iPix2Pix [7] and Stable Diffusion inpainting [48]. Our method can more accurately replicate the distortion effects caused by light refraction.

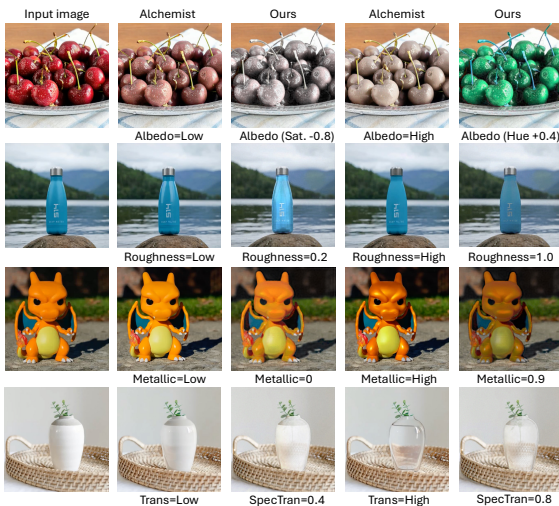


Figure 10. Qualitative evaluation of material editing. Our method enables albedo editing to various colors, whereas Alchemist [53] is limited to white. For roughness editing, our approach follows physical principles—when roughness is set to 0.2, a realistic reflection of the stone appears at the bottom of the bottle. Our method preserves Charizard’s color during metallic edits and shows that increasing metallic alone darkens the material. In transparency editing, our approach accurately captures light refraction and maintains the vase’s appearance when transparency is increased.

for each image to improve optimization. Results are shown in Fig. 10. Detailed settings and user study are provided in the supplementary material.

4.5. Human Face Relighting

We also tested the performance of our method on human face relighting to demonstrate its potential. We used Material Net, trained on the indoor dataset and not specifically optimized for the human face dataset, to predict the \mathbf{A} , \mathbf{R} , \mathbf{M} , followed by progressive optimization. The optimized results were used to relit. It is important to note that, despite the seemingly good results (as shown in Figure 11), we did not model the subsurface scattering, which is critical for realis-

tic face rendering. In our approach, subsurface scattering component is fixed within the albedo during optimization and does not change with lighting, thus making the rendered results inaccurate. This could be possibly improved in future work by integrating subsurface scattering into the rendering pipeline. Additionally, if there are specular highlights on the face, they too would be fixed in the albedo during the optimization process.

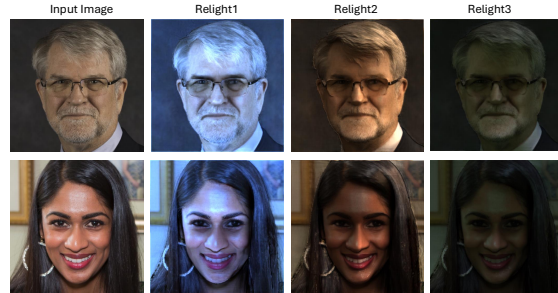


Figure 11. Our method was applied to relight real human faces (FFHQ). When the face lacks strong highlights, the relighting results are more accurate (above). However, in cases where highlights are present (below), these highlights tend to be baked into the albedo during optimization, causing them to persist even after the lighting conditions are altered.

5. Ablations

We tested the results of envmap optimization under two conditions: providing MatNet predictions versus setting $\mathbf{A} = \mathbf{R} = 0.5, \mathbf{M} = 0.1$. As shown in Table 3, providing MatNet predictions significantly improves the accuracy of envmap optimization.

We also conducted an ablation study on the value of δ in Eq. 19. Using 20 randomly selected images from the IIW dataset [4], we tested different δ values and compared the rerendered images with the input images. We evaluated two strategies: simultaneous optimization of \mathbf{A} , \mathbf{R} , \mathbf{M} and sequential optimization (\mathbf{R} , \mathbf{M} & \mathbf{A}), where \mathbf{R} , \mathbf{M} is optimized first, followed by \mathbf{A} . To save time, we applied early stopping, halting optimization if \mathcal{L}_{re} reduced by less than 5% over 20 consecutive steps. Results are shown in Table 4. For additional studies, see the supplementary material.

6. Limitations and Discussion

Since our images are rendered and mesh reconstruction limitations can cause artifacts along object edges, using super-resolution (SR) [48, 59, 65, 66] may help reduce these artifacts. However, SR models often overly modify the image, as shown in Fig. 12. Improving SR models by giving additional input could potentially mitigate this issue.

Finally, *physically based* in this paper refers to physically based rendering (PBR), a computer graphics approach that

Table 4. Ablation of δ in Eq. 19. Comparing the re-render error.

| δ | Opt ARM | | | Opt RM&A | | |
|----------|-----------------|-----------------|------------------|-----------------|-----------------|------------------|
| | SSIM \uparrow | PSNR \uparrow | MSE \downarrow | SSIM \uparrow | PSNR \uparrow | MSE \downarrow |
| 0.0 | 0.459 | 13.479 | 0.0504 | 0.611 | 17.390 | 0.0342 |
| 0.5 | 0.473 | 14.490 | 0.0473 | 0.699 | 18.242 | 0.0271 |
| 1.0 | 0.542 | 15.363 | 0.0426 | 0.618 | 17.396 | 0.0312 |
| 1.5 | 0.554 | 15.403 | 0.0446 | 0.637 | 17.541 | 0.0313 |
| 2.0 | 0.571 | 15.320 | 0.0424 | 0.640 | 17.719 | 0.0280 |
| 2.5 | 0.610 | 16.151 | 0.0371 | 0.640 | 16.922 | 0.0304 |
| 3.0 | 0.612 | 16.109 | 0.0366 | 0.656 | 16.819 | 0.0299 |

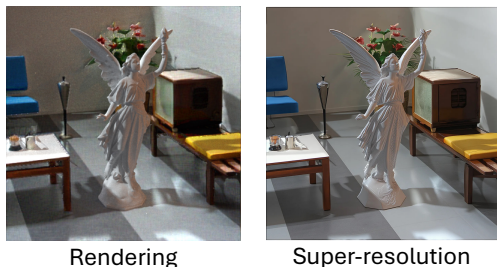


Figure 12. Super-resolution can improve image quality while preserving overall structure, such as lighting and shadows. However, Stable Diffusion-based super-resolution may alter some details, as seen in the excessive modifications to the statue in the right image.

may not strictly follow physical laws. For more general limitations, please refer to the supplementary material.

7. Conclusion

In this work, we present a novel pipeline for physically-based inverse rendering that combines neural network predictions with differentiable rendering to optimize material properties and lighting conditions from a single image. Our approach enables accurate relighting, transparent object insertion, and material editing tasks, including transparency editing without requiring complete geometry.

References

- [1] Dejan Azinovic, Tzu-Mao Li, Anton Kaplanyan, and Matthias Nießner. Inverse path tracing for joint material and lighting estimation. In *Proceedings of Computer Vision and Pattern Recognition (CVPR)*, pages 2447–2456. IEEE, 2019. 1, 2
- [2] Jingzhi Bao, Guanying Chen, and Shuguang Cui. Photometric inverse rendering: Shading cues modeling and surface reflectance regularization. arXiv:2408.06828 [cs.CV], 2024. 1, 2
- [3] Connelly Barnes, Eli Shechtman, Adam Finkelstein, and Dan B. Goldman. PatchMatch: A randomized correspondence algorithm for structural image editing. *ACM Transactions on Graphics*, 28(3):24, 2009. 1
- [4] Sean Bell, Kavita Bala, and Noah Snavely. Intrinsic images in the wild. *ACM Transactions on Graphics*, 33(4):159, 2014. 1, 6, 7, 8
- [5] Shariq Farooq Bhat, Reiner Birkel, Diana Wofk, Peter Wonka, and Matthias Müller. ZoeDepth: Zero-shot transfer by combining relative and metric depth. arXiv:2302.12288 [cs.CV], 2023. 3
- [6] Reiner Birkel, Diana Wofk, and Matthias Müller. MiDaS v3.1 – a model zoo for robust monocular relative depth estimation. arXiv:2307.14460 [cs.CV], 2023. 3
- [7] Tim Brooks, Aleksander Holynski, and Alexei A. Efros. InstructPix2Pix: Learning to follow image editing instructions. In *Proceedings of Computer Vision and Pattern Recognition (CVPR)*, pages 18392–18402. IEEE, 2023. 1, 2, 7, 8
- [8] Brent Burley. Physically-based shading at Disney. In *Practical Physically Based Shading in Film and Game Production*. ACM SIGGRAPH 2012 Courses, 2012. 4
- [9] Brent Burley. Extending the Disney BRDF to a BSDF with integrated subsurface scattering. In *Physically Based Shading in Theory and Practice*. ACM SIGGRAPH 2015 Courses, 2015. 4, 5
- [10] Wenzheng Chen, Jun Gao, Huan Ling, Edward Smith, Jaakko Lehtinen, Alec Jacobson, and Sanja Fidler. Learning to predict 3D objects with an interpolation-based differentiable renderer. In *Advances in Neural Information Processing Systems 32 (NeurIPS 2019)*, 2019. 2
- [11] Wenzheng Chen, Joey Litalien, Jun Gao, Zian Wang, Clement Fuji Tsang, Sameh Khamis, Or Litany, and Sanja Fidler. DIB-R++: learning to predict lighting and material with a hybrid differentiable renderer. In *Advances in Neural Information Processing Systems 34 (NeurIPS 2021)*, 2021. 2
- [12] JunYong Choi, SeokYeong Lee, Haesol Park, Seung-Won Jung, Ig-Jae Kim, and Junghyun Cho. MAIR: multi-view attention inverse rendering with 3d spatially-varying lighting estimation. In *Proceedings of Computer Vision and Pattern Recognition (CVPR)*, pages 8392–8401. IEEE, 2023. 2, 6, 7
- [13] Mohammad Reza Karimi Dastjerdi, Jonathan Eisenmann, Yannick Hold-Geoffroy, and Jean-François Lalonde. EverLight: Indoor-outdoor editable HDR lighting estimation. In *Proceedings of International Conference on Computer Vision (ICCV)*, pages 7420–7429. IEEE, 2023. 2
- [14] Xi Deng, Fujun Luan, Bruce Walter, Kavita Bala, and Steve Marschner. Reconstructing translucent objects using differentiable rendering. In *ACM SIGGRAPH 2022 Conference Proceedings*, pages 38:1–38:10. ACM, 2022. 2
- [15] David Eigen, Christian Puhrsch, and Rob Fergus. Depth map prediction from a single image using a multi-scale deep network. In *Advances in Neural Information Processing Systems 27 (NeurIPS 2014)*, 2014. 3
- [16] Yuto Enyo and Ko Nishino. Diffusion reflectance map: Single-image stochastic inverse rendering of illumination and reflectance. In *Proceedings of Computer Vision and Pattern Recognition (CVPR)*, pages 11873–11883. IEEE, 2024. 2
- [17] Antoine Guédon and Vincent Lepetit. Sugar: Surface-aligned gaussian splatting for efficient 3d mesh reconstruction and high-quality mesh rendering. In *Proceedings of the IEEE/CVF Conference on Computer Vision and Pattern Recognition*, pages 5354–5363, 2024. 5
- [18] Jon Hasselgren, Nikolai Hofmann, and Jacob Munkberg. Shape, light, and material decomposition from images using Monte Carlo rendering and denoising. *Advances in Neural Information Processing Systems 35 (NeurIPS 2022)*, pages 22856–22869, 2022. 2

- [19] Amir Hertz, Ron Mokady, Jay Tenenbaum, Kfir Aberman, Yael Pritch, and Daniel Cohen-Or. Prompt-to-prompt image editing with cross-attention control. In *Proceedings of International Conference on Learning Representations (ICLR)*, 2023. 1
- [20] Wenzel Jakob, Sébastien Speierer, Nicolas Roussel, Merlin Nimier-David, Delio Vicini, Tizian Zeltner, Baptiste Nicolet, Miguel Crespo, Vincent Leroy, and Ziyi Zhang. Mitsuba 3 renderer, 2022. <https://mitsuba-renderer.org>. 2
- [21] Hiroharu Kato, Deniz Beker, Mihai Morariu, Takahiro Ando, Toru Matsuoka, Wadim Kehl, and Adrien Gaidon. Differentiable rendering: A survey. arXiv:2006.12057 [cs.CV], 2020. 2
- [22] Douglas Scott Kay and Donald Greenberg. Transparency for computer synthesized images. *Computer Graphics (SIGGRAPH '79)*, 13(2):158–164, 1979. 5
- [23] Bernhard Kerbl, Georgios Kopanas, Thomas Leimkühler, and George Drettakis. 3d gaussian splatting for real-time radiance field rendering. *ACM Trans. Graph.*, 42(4):139–1, 2023. 5
- [24] Peter Kocsis, Vincent Sitzmann, and Matthias Nießner. Intrinsic image diffusion for indoor single-view material estimation. In *Proceedings of Computer Vision and Pattern Recognition (CVPR)*, pages 5198–5208. IEEE, 2024. 2, 3, 6, 7
- [25] Zhengqin Li, Kalyan Sunkavalli, and Manmohan Chandraker. Materials for masses: SVBRDF acquisition with a single mobile phone image. In *Proceedings of the European Conference on Computer Vision (ECCV)*, pages 72–87. Springer, 2018. 2
- [26] Zhengqin Li, Zexiang Xu, Ravi Ramamoorthi, Kalyan Sunkavalli, and Manmohan Chandraker. Learning to reconstruct shape and spatially-varying reflectance from a single image. *ACM Transactions on Graphics*, 37(6):269, 2018. 2
- [27] Zhengqin Li, Mohammad Shafiei, Ravi Ramamoorthi, Kalyan Sunkavalli, and Manmohan Chandraker. Inverse rendering for complex indoor scenes: Shape, spatially-varying lighting and SVBRDF from a single image. In *Proceedings of Computer Vision and Pattern Recognition (CVPR)*, pages 2475–2484. IEEE, 2020. 2, 7
- [28] Zhengqin Li, Ting-Wei Yu, Shen Sang, Sarah Wang, Meng Song, Yuhan Liu, Yu-Ying Yeh, Rui Zhu, Nitesh Gundavarapu, Jia Shi, Sai Bi, Hong-Xing Yu, Zexiang Xu, Kalyan Sunkavalli, Milos Hasan, Ravi Ramamoorthi, and Manmohan Chandraker. OpenRooms: An open framework for photorealistic indoor scene datasets. In *Proceedings of Computer Vision and Pattern Recognition (CVPR)*, pages 7190–7199. IEEE, 2021. 1, 6
- [29] Zhengqin Li, Jia Shi, Sai Bi, Rui Zhu, Kalyan Sunkavalli, Miloš Hašan, Zexiang Xu, Ravi Ramamoorthi, and Manmohan Chandraker. Physically-based editing of indoor scene lighting from a single image. In *European Conference on Computer Vision (ECCV)*, pages 555–572. Springer, 2022. 1, 2, 7
- [30] Zhen Li, Lingli Wang, Mofang Cheng, Cihui Pan, and Jiaqi Yang. Multi-view inverse rendering for large-scale real-world indoor scenes. In *Proceedings of Computer Vision and Pattern Recognition (CVPR)*, pages 12499–12509. IEEE, 2023. 1, 2
- [31] Yuan Liu, Cheng Lin, Zijiao Zeng, Xiaoxiao Long, Lingjie Liu, Taku Komura, and Wenping Wang. SyncDreamer: Generating multiview-consistent images from a single-view image. In *Proceedings of International Conference on Learning Representations (ICLR)*, 2024. 5, 2
- [32] Xiaoxiao Long, Yuan-Chen Guo, Cheng Lin, Yuan Liu, Zhiyang Dou, Lingjie Liu, Yuexin Ma, Song-Hai Zhang, Marc Habermann, Christian Theobalt, et al. Wonder3D: Single image to 3D using cross-domain diffusion. In *Proceedings of Computer Vision and Pattern Recognition (CVPR)*, pages 9970–9980. IEEE, 2024. 5, 2
- [33] Fujun Luan, Shuang Zhao, Kavita Bala, and Zhao Dong. Unified shape and SVBRDF recovery using differentiable Monte Carlo rendering. *Computer Graphics Forum*, 40(4):101–113, 2021. 2
- [34] Jundan Luo, Duygu Ceylan, Jae Shin Yoon, Nanxuan Zhao, Julien Philip, Anna Frühstück, Wenbin Li, Christian Richardt, and Tuanfeng Wang. IntrinsicDiffusion: joint intrinsic layers from latent diffusion models. In *ACM SIGGRAPH 2024 Conference Papers*, pages 74:1–74:11. ACM, 2024. 2
- [35] Linjie Lyu, Ayush Tewari, Marc Habermann, Shunsuke Saito, Michael Zollhöfer, Thomas Leimkühler, and Christian Theobalt. Diffusion posterior illumination for ambiguity-aware inverse rendering. *ACM Transactions on Graphics*, 42(6):233, 2023. 2, 6, 7
- [36] Chenlin Meng, Yutong He, Yang Song, Jiaming Song, Jiajun Wu, Jun-Yan Zhu, and Stefano Ermon. SDEdit: Guided image synthesis and editing with stochastic differential equations. In *Proceedings of International Conference on Learning Representations (ICLR)*, 2021. 1
- [37] Ben Mildenhall, Pratul P. Srinivasan, Matthew Tancik, Jonathan T. Barron, Ravi Ramamoorthi, and Ren Ng. NeRF: Representing scenes as neural radiance fields for view synthesis. *Communications of the ACM*, 65(1):99–106, 2021. 2, 4, 5
- [38] Ron Mokady, Amir Hertz, Kfir Aberman, Yael Pritch, and Daniel Cohen-Or. Null-text inversion for editing real images using guided diffusion models. In *Proceedings of Computer Vision and Pattern Recognition (CVPR)*, pages 6038–6047. IEEE, 2023. 1, 2
- [39] Maxime Oquab, Timothée Darcet, Theo Moutakanni, Huy V. Vo, Marc Szafraniec, Vasil Khalidov, Pierre Fernandez, Daniel Haziza, Francisco Massa, Alaaeldin El-Nouby, Russell Howes, Po-Yao Huang, Hu Xu, Vasu Sharma, Shang-Wen Li, Wojciech Galuba, Mike Rabbat, Mido Assran, Nicolas Ballas, Gabriel Synnaeve, Ishan Misra, Herve Jegou, Julien Mairal, Patrick Labatut, Armand Joulin, and Piotr Bojanowski. DINOv2: Learning robust visual features without supervision. *Transactions on Machine Learning Research*, 2024. 3
- [40] Xingang Pan, Ayush Tewari, Thomas Leimkühler, Lingjie Liu, Abhimitra Meka, and Christian Theobalt. Drag your gan: Interactive point-based manipulation on the generative image manifold. In *ACM SIGGRAPH 2023 Conference Proceedings*, pages 78:1–78:11. ACM, 2023. 1
- [41] Rohit Pandey, Sergio Orts-Escolano, Chloe Legendre, Christian Haene, Sofien Bouaziz, Christoph Rhemann, Paul E. Debevec, and Sean Ryan Fanello. Total relighting: learning to relight portraits for background replacement. *ACM Transactions on Graphics*, 40(4):43, 2021. 2

- [42] Jeong Joon Park, Aleksander Holynski, and Steven M Seitz. Seeing the world in a bag of chips. In *Proceedings of Computer Vision and Pattern Recognition (CVPR)*, pages 1417–1427. IEEE, 2020. 2, 6
- [43] Steven G. Parker, James Bigler, Andreas Dietrich, Heiko Friedrich, Jared Hoberock, David Luebke, David McAllister, Morgan McGuire, Keith Morley, Austin Robison, and Martin Stich. OptiX: a general purpose ray tracing engine. *ACM Transactions on Graphics*, 29(4):66, 2010. 2
- [44] Pakkapon Phongthawee, Worameth Chinchuthakun, Nontaphat Sinsunthithet, Varun Jampani, Amit Raj, Pramook Khungurn, and Supasorn Suwajanakorn. Diffusionlight: Light probes for free by painting a chrome ball. In *Proceedings of the IEEE/CVF Conference on Computer Vision and Pattern Recognition*, pages 98–108, 2024. 6, 7
- [45] Kris Papat and Rosalind W. Picard. Novel cluster-based probability model for texture synthesis, classification, and compression. In *Visual Communications and Image Processing '93*, pages 756–768. SPIE, 1993. 1
- [46] René Ranftl, Alexey Bochkovskiy, and Vladlen Koltun. Vision transformers for dense prediction. In *Proceedings of International Conference on Computer Vision (ICCV)*, pages 12179–12188. IEEE, 2021. 3
- [47] Nikhila Ravi, Valentin Gabeur, Yuan-Ting Hu, Ronghang Hu, Chaitanya Ryali, Tengyu Ma, Haitham Khedr, Roman Rädle, Chloe Rolland, Laura Gustafson, Eric Mintun, Junting Pan, Kalyan Vasudev Alwala, Nicolas Carion, Chao-Yuan Wu, Ross Girshick, Piotr Dollár, and Christoph Feichtenhofer. SAM 2: Segment anything in images and videos. arXiv:2408.00714 [cs.CV], 2024. 5
- [48] Robin Rombach, Andreas Blattmann, Dominik Lorenz, Patrick Esser, and Björn Ommer. High-resolution image synthesis with latent diffusion models. In *Proceedings of Computer Vision and Pattern Recognition (CVPR)*, pages 10684–10695. IEEE, 2022. 1, 2, 3, 5, 7, 8
- [49] Shen Sang and Manmohan Chandraker. Single-shot neural relighting and SVBRDF estimation. In *European Conference on Computer Vision (ECCV)*, pages 85–101. Springer, 2020. 2
- [50] Ayush Sarkar, Hanlin Mai, Amitabh Mahapatra, Svetlana Lazebnik, David A Forsyth, and Anand Bhattad. Shadows don't lie and lines can't bend! Generative models don't know projective geometry... for now. In *Proceedings of Computer Vision and Pattern Recognition (CVPR)*, pages 28140–28149. IEEE, 2024. 3
- [51] Christophe Schlick. An inexpensive BRDF model for physically-based rendering. *Computer Graphics Forum*, 13(3):233–246, 1994. 4
- [52] Soumyadip Sengupta, Jinwei Gu, Kihwan Kim, Guilin Liu, David W. Jacobs, and Jan Kautz. Neural inverse rendering of an indoor scene from a single image. In *Proceedings of International Conference on Computer Vision (ICCV)*, pages 8598–8607. IEEE, 2019. 1, 2
- [53] Prafull Sharma, Varun Jampani, Yuanzhen Li, Xuhui Jia, Dmitry Lagun, Fredo Durand, Bill Freeman, and Mark Matthews. Alchemist: Parametric control of material properties with diffusion models. In *Proceedings of Computer Vision and Pattern Recognition (CVPR)*, pages 24130–24141. IEEE, 2024. 1, 2, 7, 8, 3, 4
- [54] Ruoxi Shi, Hansheng Chen, Zhuoyang Zhang, Minghua Liu, Chao Xu, Xinyue Wei, Linghao Chen, Chong Zeng, and Hao Su. Zero123++: a single image to consistent multi-view diffusion base model. arXiv:2310.15110 [cs.CV], 2023. 5, 2
- [55] Yujun Shi, Chuhui Xue, Jun Hao Liew, Jiachun Pan, Hanshu Yan, Wenqing Zhang, Vincent YF Tan, and Song Bai. Dragdiffusion: Harnessing diffusion models for interactive point-based image editing. In *Proceedings of Computer Vision and Pattern Recognition (CVPR)*, pages 8839–8849. IEEE, 2024. 2
- [56] Cheng Sun, Guangyan Cai, Zhengqin Li, Kai Yan, Cheng Zhang, Carl Marshall, Jia-Bin Huang, Shuang Zhao, and Zhao Dong. Neural-PBIR reconstruction of shape, material, and illumination. In *Proceedings of International Conference on Computer Vision (ICCV)*, pages 18046–18056. IEEE, 2023. 2
- [57] Tristan Swedish, Connor Henley, and Ramesh Raskar. Objects as cameras: Estimating high-frequency illumination from shadows. In *Proceedings of International Conference on Computer Vision (ICCV)*, pages 2593–2602. IEEE, 2021. 2
- [58] Jiajun Tang, Yongjie Zhu, Haoyu Wang, Jun Hoong Chan, Si Li, and Boxin Shi. Estimating spatially-varying lighting in urban scenes with disentangled representation. In *European Conference on Computer Vision (ECCV)*, pages 454–469. Springer, 2022. 2
- [59] Jasper AI Team. Flux.1-dev: Upscaler ControlNet. <https://huggingface.co/jasperai/Flux.1-dev-Controlnet-Upscaler>, 2024. Accessed 13 November 2024. 8
- [60] Dor Verbin, Ben Mildenhall, Peter Hedman, Jonathan T. Barron, Todd Zickler, and Pratul P. Srinivasan. Eclipse: Disambiguating illumination and materials using unintended shadows. In *Proceedings of Computer Vision and Pattern Recognition (CVPR)*, pages 77–86. IEEE, 2024. 2, 6
- [61] Bruce Walter, Stephen R. Marschner, Hongsong Li, and Kenneth E. Torrance. Microfacet models for refraction through rough surfaces. In *Proceedings of Eurographics Symposium on Rendering (EGSR)*, pages 195–206. Eurographics Association, 2007. 4
- [62] Guangcong Wang, Yinuo Yang, Chen Change Loy, and Ziwei Liu. Stylelight: Hdr panorama generation for lighting estimation and editing. In *European Conference on Computer Vision (ECCV)*, pages 477–492. Springer, 2022. 2
- [63] Lezhong Wang, Jeppe Revall Frisvad, Mark Bo Jensen, and Siavash Arjomand Bigdeli. StereoDiffusion: Training-free stereo image generation using latent diffusion models. In *Proceedings of Computer Vision and Pattern Recognition Workshop (CVPRW)*, pages 7416–7425. IEEE, 2024. 2
- [64] Peng Wang, Lingjie Liu, Yuan Liu, Christian Theobalt, Taku Komura, and Wenping Wang. NeuS: Learning neural implicit surfaces by volume rendering for multi-view reconstruction. In *Advances in Neural Information Processing Systems 34 (NeurIPS 2021)*, 2021. 2
- [65] Xintao Wang, Liangbin Xie, Chao Dong, and Ying Shan. Real-esrgan: Training real-world blind super-resolution with

- pure synthetic data. In *Proceedings of International Conference on Computer Vision (ICCV)*, pages 1905–1914. IEEE, 2021. [8](#)
- [66] Kailu Wu, Fangfu Liu, Zhihan Cai, Runjie Yan, Hanyang Wang, Yating Hu, Yueqi Duan, and Kaisheng Ma. Unique3D: High-quality and efficient 3D mesh generation from a single image. *arXiv:2405.20343 [cs.CV]*, 2024. [8](#)
- [67] Liwen Wu, Rui Zhu, Mustafa B Yaldiz, Yin hao Zhu, Hong Cai, Janarбек Matai, Fatih Porikli, Tzu-Mao Li, Manmohan Chandraker, and Ravi Ramamoorthi. Factorized inverse path tracing for efficient and accurate material-lighting estimation. In *Proceedings of International Conference on Computer Vision (ICCV)*, pages 3848–3858. IEEE, 2023. [1](#), [2](#)
- [68] Lihe Yang, Bingyi Kang, Zilong Huang, Xiaogang Xu, Jiashi Feng, and Hengshuang Zhao. Depth anything: Unleashing the power of large-scale unlabeled data. In *Proceedings of Computer Vision and Pattern Recognition (CVPR)*, pages 10371–10381. IEEE, 2024. [3](#)
- [69] Yao Yao, Jingyang Zhang, Jingbo Liu, Yihang Qu, Tian Fang, David McKinnon, Yang hai Tsin, and Long Quan. NeILF: Neural incident light field for physically-based material estimation. In *European Conference on Computer Vision (ECCV)*, pages 700–716. Springer, 2022. [1](#), [2](#), [6](#)
- [70] Yu-Ying Yeh, Koki Nagano, Sameh Khamis, Jan Kautz, Ming-Yu Liu, and Ting-Chun Wang. Learning to relight portrait images via a virtual light stage and synthetic-to-real adaptation. *ACM Transactions on Graphics*, 41(6):231, 2022. [2](#)
- [71] Bohan Yu, Siqi Yang, Xuanning Cui, Siyan Dong, Baoquan Chen, and Boxin Shi. MLO: Multi-bounce inverse rendering for indoor scene with light-emitting objects. *IEEE Transactions on Pattern Analysis and Machine Intelligence*, 45(8): 10129–10142, 2023. [1](#), [2](#)
- [72] Hong-Xing Yu, Samir Agarwala, Charles Herrmann, Richard Szeliski, Noah Snavely, Jiajun Wu, and Deqing Sun. Accidental light probes. In *Proceedings of Computer Vision and Pattern Recognition (CVPR)*, pages 12521–12530. IEEE, 2023. [2](#), [6](#)
- [73] Zehao Yu, Songyou Peng, Michael Niemeyer, Torsten Sattler, and Andreas Geiger. MonoSDF: Exploring monocular geometric cues for neural implicit surface reconstruction. In *Advances in Neural Information Processing Systems 35 (NeurIPS 2022)*, pages 25018–25032, 2022. [2](#)
- [74] Zehao Yu, Anpei Chen, Binbin Huang, Torsten Sattler, and Andreas Geiger. Mip-splatting: Alias-free 3d gaussian splatting. In *Proceedings of the IEEE/CVF Conference on Computer Vision and Pattern Recognition*, pages 19447–19456, 2024. [5](#)
- [75] Cheng Zhang, Zihan Yu, and Shuang Zhao. Path-space differentiable rendering of participating media. *ACM Transactions on Graphics*, 40(4):76, 2021. [2](#)
- [76] Kai Zhang, Fujun Luan, Zhengqi Li, and Noah Snavely. IRON: Inverse rendering by optimizing neural SDFs and materials from photometric images. In *Proceedings of Computer Vision and Pattern Recognition (CVPR)*, pages 5565–5574. IEEE, 2022. [2](#)
- [77] Lvmin Zhang, Anyi Rao, and Maneesh Agrawala. Ic-light github page, 2024. [1](#)
- [78] Jingsen Zhu, Fujun Luan, Yuchi Huo, Zihao Lin, Zhihua Zhong, Dianbing Xi, Rui Wang, Hujun Bao, Jiayang Zheng, and Rui Tang. Learning-based inverse rendering of complex indoor scenes with differentiable Monte Carlo raytracing. In *SIGGRAPH Asia 2022 Conference Papers*, pages 6:1–6:8. ACM, 2022. [2](#), [6](#), [7](#), [1](#)
- [79] Rui Zhu, Zhengqin Li, Janarбек Matai, Fatih Porikli, and Manmohan Chandraker. IRISformer: Dense vision transformers for single-image inverse rendering in indoor scenes. In *Proceedings of Computer Vision and Pattern Recognition (CVPR)*, pages 2822–2831. IEEE, 2022. [1](#), [2](#), [3](#)

Materialist: Physically Based Editing Using Single-Image Inverse Rendering

Supplementary Material

8. More Ablations

Here we provide more ablation results.

8.1. Optimize SH coefficients instead of envmap

We tested using SH coefficients instead of envmaps and found that optimizing SH coefficients took longer to reach the same loss. We use 3rd-order SH coefficients to represent the light source. Given the ground truth material properties, we perform light source optimization under different lighting conditions. The time taken by each method to achieve the same \mathcal{L}_{re} is compared. The results is shown if Table 5.

Table 5. Time taken by different methods to optimize \mathcal{L}_{re} to 0.03. Direct envmap optimization is faster than optimize SH coefficient.

| | SH coeff | Envmap |
|------|----------|--------|
| Time | 473 s | 103 s |

8.2. Optimization Steps and Rerendering error

We analyzed the relationship between optimization steps and rerender error. We randomly selected 10 images from the InteriorVerse dataset [78] to test rerendering error at different optimization steps. Optimization on an RTX 3090 runs at 2 steps per second. Based on MatNet’s accuracy, satisfactory results are typically achieved after 10 minutes of optimization. Results are shown in Table. 6.

Table 6. Ablation of Optimization steps. Compare the rerender error.

| Opt Steps | SSIM \uparrow | PSNR \uparrow | MSE \downarrow |
|-----------|-----------------|-----------------|------------------|
| 50 | 0.645 | 15.529 | 0.0180 |
| 100 | 0.750 | 18.735 | 0.0134 |
| 1000 | 0.825 | 25.675 | 0.0034 |
| 2000 | 0.876 | 28.204 | 0.0015 |

8.3. Optimization Network

We experimented with using a CNN-based UNet for Material Properties optimization. The UNet architecture includes 2 downsampling blocks and 2 upsampling blocks, with each block containing two 2D convolution layers (kernel size = 3, padding = 1). Additionally, we compared direct optimization of material properties without a neural network. As shown in Fig. 13, direct optimization was the slowest, followed by the CNN-based UNet, while the position-embedded MLP achieved the fastest optimization speed.

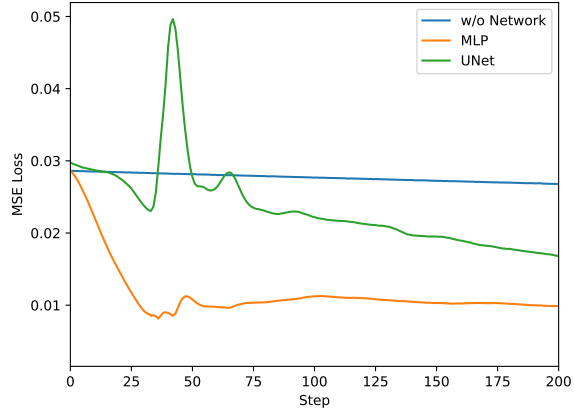


Figure 13. Compared to a CNN-based UNet, the position-embedded MLP achieves faster optimization.

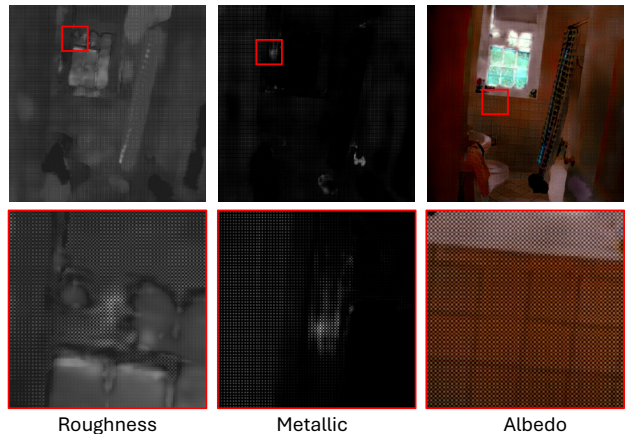


Figure 14. UNet Artifact. The red box highlights an enlarged view of this area, and the details is in the second row.

Additionally, due to the characteristics of convolutional neural networks, noticeable artifacts may appear during optimization. As shown in Fig. 14, the optimized images show a regular pattern of black dots.

It is worth noting that when MatNet predictions are unreliable (e.g., for roughness and metallic), directly optimizing material properties without relying on the neural network can achieve lower \mathcal{L}_{re} given sufficient optimization time (such as more than 3000 optimization steps). Table 7 shows the minimum MSE render loss achievable by both methods in the absence of roughness and metallic predictions.

Table 7. Comparison of the lowest \mathcal{L}_{re} that can be obtained using MLP and directly optimizing material properties when the predicted roughness and metallic are not provided.

| | w/o Network | w/ MLP |
|------------------------|-------------|--------|
| Min \mathcal{L}_{re} | 0.0038 | 0.0087 |

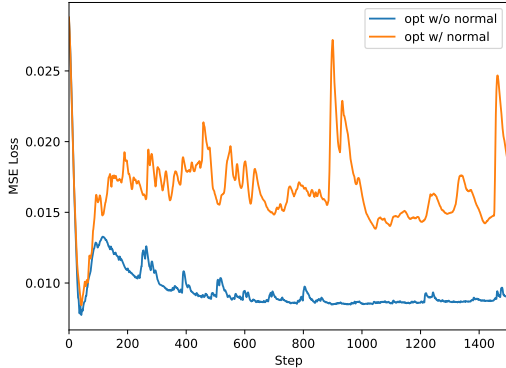


Figure 15. Optimizing normal at the same time will make the optimization process more unstable.

8.4. Optimizing Normal

As shown in Fig. 15, optimizing material properties while simultaneously optimizing normals often leads to convergence difficulties. To address this, directly optimizing normals without relying on a neural network can help mitigate these issues.

9. Limitations

In this section, we discuss potential limitations of our proposed method from a broader, user-oriented perspective. It is important to note that some points, such as the need for per-image optimization, are not typically viewed as limitations within the differentiable rendering field. However, from a user’s viewpoint, this may make our approach less convenient than stable diffusion-based methods [7, 53].

1. As with all differentiable rendering methods, our approach requires optimization for each image to obtain the lighting and optimized material properties, which might be quite time-consuming. Depending on MatNet’s prediction accuracy, optimization takes between 5 to 30 minutes. For out-of-domain images (i.e., non-indoor scenes) or higher-quality requirements, optimization time may increase. This limits our method’s ability to achieve the rapid, batch image editing enabled by stable diffusion-based techniques [7]. Training MatNet on a broader dataset for more accurate predictions could help mitigate this limitation.

2. Our method uses an envmap to represent lighting,

complicating accurate modeling of physical light sources in the scene. If a light source is present in the original image, optimization may fix it within the albedo, leading to inaccuracies during relighting.

3. The introduction of differentiable rendering allows our method to perform well even on out-of-domain images. However, if MatNet predictions are poor, differential rendering optimization requires careful tuning for each image, such as adding a mask to the object to be edited or experimenting with different optimization strategies.

4. For Material Transparency Editing, complex object geometry can lead to inaccurate refraction distortions, as our method assumes only two refractions. Single-view mesh reconstruction [31, 32, 54] may yield more accurate refractions for complex shapes. Besides, since we simulate refraction without the rays truly passing through the object, shadows cast by transparent objects may lack accuracy, and does not have caustic effect. (Note that this problem does not exist for object insertion tasks with complete geometry.)

5. Due to mesh reconstruction limitations, artifacts may appear along object edges during strong relighting, as the mesh is discontinuous at these edges. This can be mitigated using super resolution.

6. For images with transparent objects, super-resolution often yields unreliable results and may require multiple samples to reach an acceptable outcome, as shown in Fig. 16. (This is not a limitation of our method, but is noted here due to the potential need for SR techniques.)

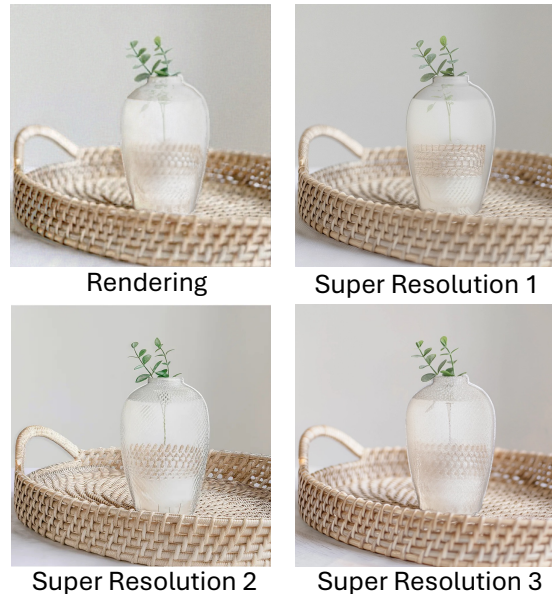


Figure 16. Super-resolution often struggles with refraction effects. As shown, both Super Resolution 1 and Super Resolution 2 exhibit noticeable refraction issues, requiring multiple runs to achieve a satisfactory result, as seen in Super Resolution 3.

10. Refraction Length Prediction

Refraction plays a critical role in visual accuracy in physically based rendering. Our pipeline is fine tuned for single view material and geometric estimation. This however means that information behind a reflective/refractive interface is intractable from a single view without any additional geometric information. Furthermore, this also means that objects cannot be edited accurately when secondary interfaces are crucial to the visual fidelity. To overcome this issue we train another neural network essential to predict secondary refractive interfaces if a user wants to change any material to transparent object such as glass, water etc. We describe this pipeline in this section.

10.1. Dataset Preparation

To create a dataset to predict the secondary interface distance, we collected a set of 200 environment maps, 50 triangle meshes of objects commonly found in the indoors environments like cups, fruits etc. Next we predefined a set of 200 viewpoints that generally covers the entire exterior surface of an object.

The data collection was done in 2 parts, first the set of 200 environment maps were rendered without any object in the scene which illustrates the background of the scene. This dataset was 200 (Environment maps) \times 200 (Viewpoints) images in quantity. The second part of the data collection was done in scenes without an environment map, where the objects were placed in the center of the scene and the 200 viewpoints were used to capture the distance to the secondary interface if the object were to be transparent. The distances can be generally defined as,

$$d = \begin{cases} \|\mathcal{P}_{n+1} - \mathcal{P}_n\|, & \text{if } \vec{\omega}_r \cdot \vec{n} > 0 \text{ \& hollow object} \\ \|\mathcal{P}_{n+1} - \mathcal{P}_n\|, & \text{if } \vec{\omega}_r \cdot \vec{n} < 0 \text{ \& non-hollow object} \\ 0, & \text{Otherwise} \end{cases} \quad (24)$$

where,

- \mathcal{P}_n : is the n -th intersection point in 3D world coordinates,
- $\vec{\omega}_r \cdot \vec{n}$: is the cosine term of the ray direction $\vec{\omega}_r$ and the normal \vec{n} .

Furthermore, "hollow" objects represent things like water jugs with air in between the surfaces and "non-hollow" objects are things like lemon with no air inside the object.

Examples are shown in Fig. 17.

11. Material Editing Settings

The selected images are out-of-domain for the indoor dataset, resulting in MatNet predictions where only albedo is relatively accurate, while roughness and metallic predictions are poor and unsuitable as initial conditions for optimization.

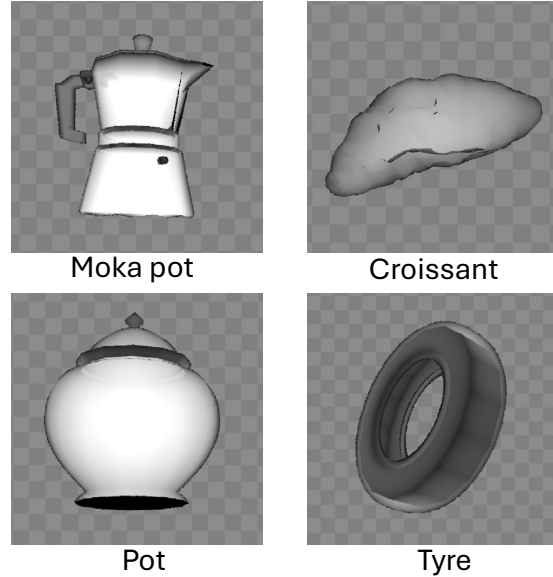


Figure 17. Example of refraction length dataset. The closer to white, the longer the refraction distance.

Therefore, specific optimization conditions must be set for each image to achieve satisfactory results.

Cherry. The predicted roughness and metallic are relatively inaccurate, leading to excessive red light in the envmap if directly used for optimization. To address this, we initialize the envmap as pure white and start with material property optimization. The default initial values for roughness and metallic are set to 0.5. After optimizing roughness and metallic, we proceed to envmap optimization, followed by albedo optimization, as albedo predictions are more reliable.

Bottle. MatNet predictions are relatively accurate, and optimization follows the method described in the main paper.

Charizard and Vase. Similar to Cherry, we initialize the envmap as pure white and start with material property optimization. Roughness and metallic are initialized to 0.5, while albedo uses MatNet predictions. Optimization begins with roughness and metallic, followed by envmap optimization, and finally albedo optimization. During editing, setting all mask values uniformly for metallic without adjusting roughness can introduce artifacts. To improve material editing results, we use a mask during optimization. Specifically, SAM2 is used to segment Charizard's and vase's mask, roughness and metallic values are unified within the mask during optimization. This ensures better editing results.

12. Material Editing User Study

We conducted a user study on material editing results, asking participants to rank the editing results from Alchemist [53], ours (direct rendering), and ours SR (rendered result refined with Super Resolution). The highest rank received

3 points, and the lowest 1 point. Since these are real-world photos with no ground truth, participants were provided with synthetic scene renderings as reference and asked to imagine the expected edit on real photos as closely as possible. It should be noted that participants generally found it challenging to envision the correct editing result, making it difficult to judge which method was better. When uncertain, participants often zoomed in to examine details for ranking, which may have led to lower scores for our direct rendering. However, our scores improved significantly after applying super resolution.

Table 8. Material Editing User Study. SR represent for super resolution.

| Edit Task | Alchemist [53] | Ours | Ours (SR) |
|-----------|----------------|------|-------------|
| Albedo | 1.04 | 2.36 | 2.61 |
| Roughness | 2.21 | 1.57 | 2.21 |
| Metallic | 2.50 | 1.79 | 1.71 |
| Trans | 1.93 | 1.64 | 2.43 |
| Sum | 7.68 | 7.36 | 8.96 |

13. Coordinate Transformation

Since our input into the renderer are based in screen space, we briefly describe how to transform a world-position \mathbf{x} into screen-space. Extending \mathbf{x} into homogeneous coordinates $\mathbf{W} = [x, y, z, 1]^T$, we first transform into camera space coordinates by

$$\mathbf{Q} = E^{-1} \cdot \mathbf{W} \tag{25}$$

where E is the extrinsic camera matrix. For a perspective projection matrix \mathbf{P} we can obtain the Normalized Device Coordinates (NDC) by:

$$\mathbf{N} = \mathbf{P} \cdot \mathbf{Q} \tag{26}$$

Converting \mathbf{N} into inhomogeneous coordinates we can obtain the screen-space coordinates:

$$\begin{aligned} x_{\text{screen}} &= \left(\frac{x_{\text{ndc}} + 1}{2} \right) \cdot W \\ y_{\text{screen}} &= \left(\frac{y_{\text{ndc}} + 1}{2} \right) \cdot H \end{aligned} \tag{27}$$

This process maps the world position to a specific location on the screen which we will denote as $\mathbf{x}_s = \mathbf{S}(\mathbf{x}) = [x_{\text{screen}}, y_{\text{screen}}]$. In the following \mathbf{A} , \mathbf{R} and \mathbf{M} represents the image texture values of albedo, roughness and metallic. Thus for a shading point \mathbf{x} , we can obtain the material properties with screen coordinate indexing i.e. $\mathbf{A}(\mathbf{x}_s)$, $\mathbf{R}(\mathbf{x}_s)$ and $\mathbf{M}(\mathbf{x}_s)$.

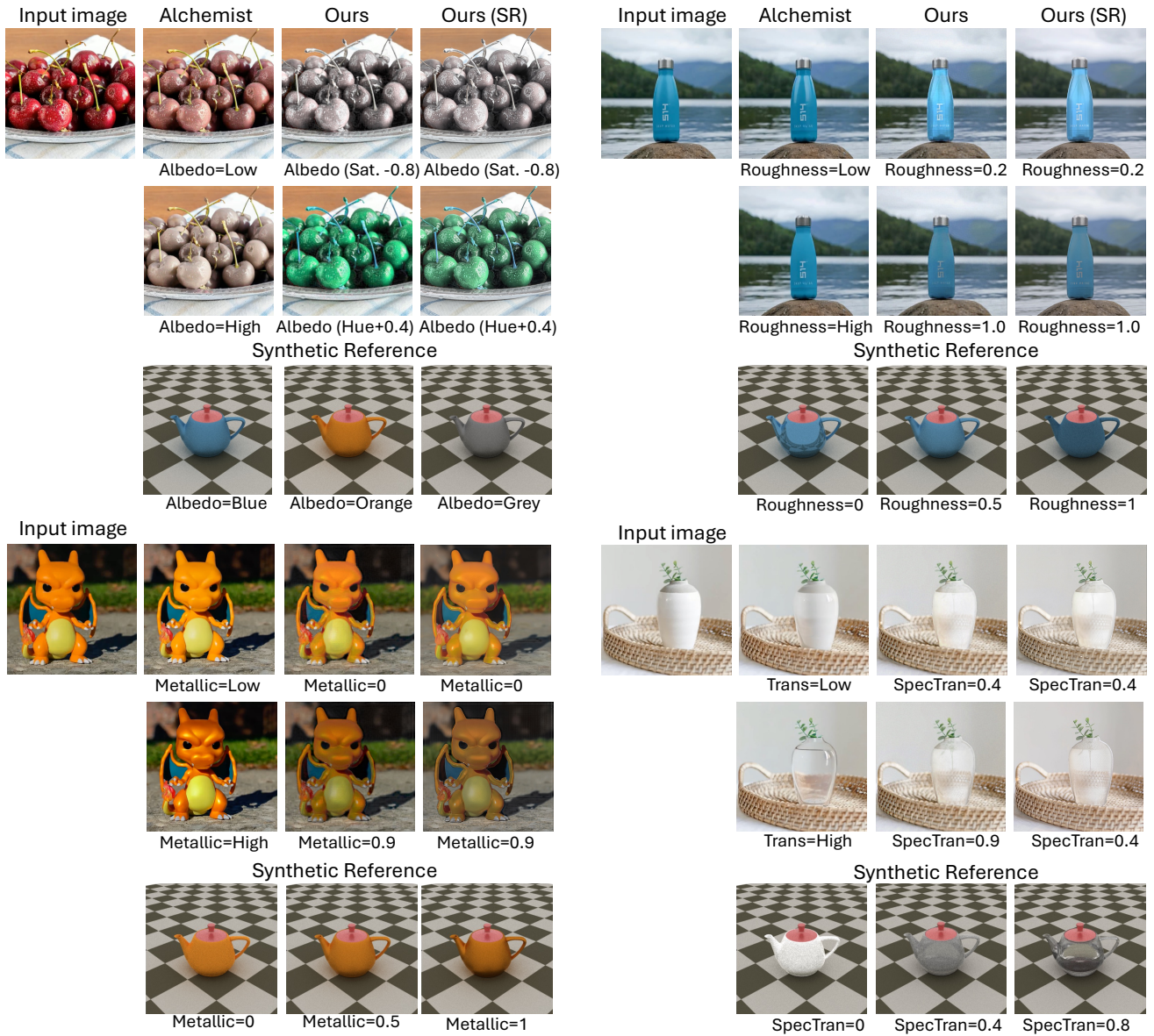


Figure 18. Our methods with super-resolution. Using super resolution (SR) can greatly improve the quality of the rendered image. However, the current SR model cannot fully retain the details of the original image and will make excessive modifications to the original image. We also provide the effect of modifications to material properties on appearance in a synthetic dataset.